



Article

Infrared Characterization of the Bidirectional Oxygen-Sensitive [NiFe]-Hydrogenase from *E. coli*

Moritz Senger^{1,†}, Konstantin Laun^{1,†}, Basem Soboh²  and Sven T. Stripp^{1,*} 

¹ Department of Physics, Experimental Molecular Biophysics, Freie Universität Berlin, 14195 Berlin, Germany; senger@zedat.fu-berlin.de (M.S.); konstantin.laun@fu-berlin.de (K.L.)

² Department of Physics, Genetic Biophysics, Freie Universität Berlin, 14195 Berlin, Germany; basem.soboh@fu-berlin.de

* Correspondence: sven.stripp@fu-berlin.de; Tel.: +49-030-838-55069

† These authors contributed equally.

Received: 16 October 2018; Accepted: 6 November 2018; Published: 8 November 2018



Abstract: [NiFe]-hydrogenases are gas-processing metalloenzymes that catalyze the conversion of dihydrogen (H₂) to protons and electrons in a broad range of microorganisms. Within the framework of green chemistry, the molecular proceedings of biological hydrogen turnover inspired the design of novel catalytic compounds for H₂ generation. The bidirectional “O₂-sensitive” [NiFe]-hydrogenase from *Escherichia coli* HYD-2 has recently been crystallized; however, a systematic infrared characterization in the presence of natural reactants is not available yet. In this study, we analyze HYD-2 from *E. coli* by in situ attenuated total reflection Fourier-transform infrared spectroscopy (ATR FTIR) under quantitative gas control. We provide an experimental assignment of all catalytically relevant redox intermediates alongside the O₂- and CO-inhibited cofactor species. Furthermore, the reactivity and mutual competition between H₂, O₂, and CO was probed in real time, which lays the foundation for a comparison with other enzymes, e.g., “O₂-tolerant” [NiFe]-hydrogenases. Surprisingly, only Ni-B was observed in the presence of O₂ with no indications for the “unready” Ni-A state. The presented work proves the capabilities of in situ ATR FTIR spectroscopy as an efficient and powerful technique for the analysis of biological macromolecules and enzymatic small molecule catalysis.

Keywords: redox enzymes; FTIR spectroscopy; small molecules

1. Introduction

Hydrogenases are gas-processing metalloenzymes that catalyze “hydrogen turnover” (H₂ ⇌ 2H⁺ + 2e[−]) in various organisms [1]. Oxidation of molecular hydrogen is typically referred to as “H₂ uptake” while proton reduction leads to “H₂ release”. Under physiological conditions, [FeFe]-hydrogenases show pronounced H₂ release activity while [Fe]- and [NiFe]-hydrogenases are typically employed in H₂ uptake [2–4]. These three classes are unrelated and differ significantly in protein fold and composition of the catalytic transition metal cofactor [5]. An understanding of the molecular proceedings of hydrogen turnover may inspire novel catalytic compounds for an industrial generation of H₂ as a fuel [6–8].

The gram-negative, facultative anaerobic bacterium *Escherichia coli* synthesizes at least three membrane-associated [NiFe]-hydrogenases [9]. Facing the cytoplasm, HYD-3 catalyzes the oxidation of formic acid into H₂ and CO₂ as part of the formate hydrogenlyase complex. HYD-1 and HYD-2 are respiratory hydrogenases of the periplasm whose hydrogen turnover activity has been suggested to be linked to the energy metabolism of the cell (HYD-2) or the reduction of trace amounts of O₂ (HYD-1) [10]. Accordingly, HYD-1 is an “O₂-tolerant” [NiFe]-hydrogenase that maintains significant

turnover activity in the presence of O₂ while HYD-2 is inhibited by O₂ and has been classified “O₂-sensitive” [11–13]. In O₂-sensitive [NiFe]-hydrogenases the structural plasticity of an iron–sulfur cluster proximal to the active site cofactor was shown to play a key role in the immediate recovery from O₂-inhibited species and reduction of O₂ under hydrogen turnover conditions [14–16].

Figure 1A depicts the recently crystallized HYD-2 heterodimer [13]. Subunit HybO (~40 kDa) carries three iron–sulfur clusters that facilitate electron exchange between redox partners and catalytic center. In difference to HYD-1 [17,18] the moiety most proximal to the [NiFe] cofactor is a conventional [4Fe-4S]-cluster. Subunit HybC (~63 kDa) binds the catalytic center in tunneling distance to the proximal iron–sulfur cluster (Figure 1B). Four conserved cysteine residues (C61/C64, C546/C549) coordinate the bimetallic [NiFe] active site. The iron ion binds two cyanide (CN[−]) and one carbon monoxide ligand (CO), which facilitates infrared (IR) spectroscopic studies on [NiFe]-hydrogenases [19]. The CO/CN[−] stretching frequencies are sensitive “reporters” for changes in electron density distribution across the cofactor and can be addressed to characterize different redox- and protonation states [20–22]. In the second coordination sphere, several homologous residues have been proposed to be involved in proton transfer between bulk water and active site cofactor. One possible trajectory includes C546 and E14 [23–25], an alternative route comprises R479, D103, and D544 [26].

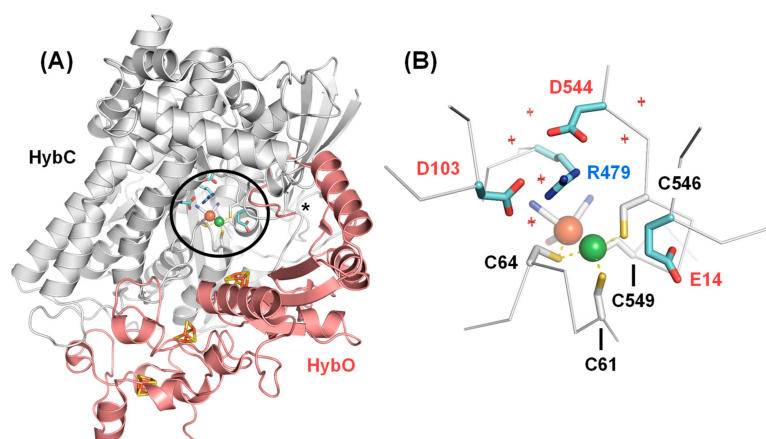


Figure 1. Crystal structure of the [NiFe]-hydrogenase HYD-2 from *E. coli* (pdb coordinates 6EHQ) [13]. (A) Subunit HybC (light grey) binds the catalytic cofactor whereas subunit HybO (red) carries three iron–sulfur clusters. In this representation HybO is truncated by 48 amino acids (*) to reveal the view onto the active site niche (black circle); (B) Catalytic cofactor including amino acids of the first and second coordination sphere (cyan) that are potentially involved in proton transfer [23–26]. Non-bonded molecules (crosses, H₂O) may be involved in proton transfer as well.

Protein crystallography, electrochemistry, EPR- and IR spectroscopy on [NiFe]-hydrogenases significantly contributed to the understanding of biological hydrogen turnover [27–30]. The H₂ uptake reaction was suggested to include 3–4 redox species (Figure 2) [20,21]. **Ni-SI** represents the active-ready, oxidized state (Ni²⁺/Fe²⁺) that stabilizes an open coordination site between nickel and iron ion (dotted circle in Figure 2). Dihydrogen reacts at the nickel ion and forms a Ni-Fe bridging hydride species in the “super-reduced” **Ni-R** state [31,32]. One proton is released in the process; for **Ni-R1**, high resolution crystallography suggested a protonated cysteine (C546 in HYD-2) [25] but protonation of R479 has also been proposed [26]. The very location of the proton in **Ni-R2** and **Ni-R3** is unclear; however, the shift to lower IR frequencies from R1 to R3 may indicate an increase in distance relative to the Fe(CN)₂CO reporter group.

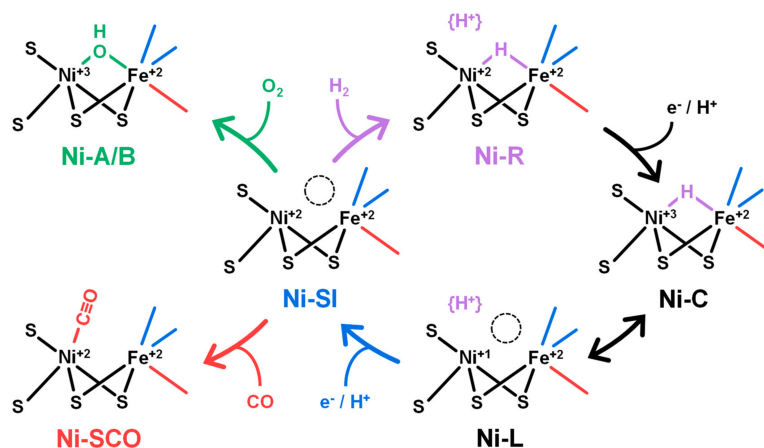


Figure 2. Intermediates of the [NiFe] cofactor and catalytic cycle [20,21]. Based on crystallographic data the cartoon shows the bimetallic cofactor as coordinated by four cysteines. The iron ion is equipped with two CN^- (blue) and one CO ligand (red). Catalytic intermediates Ni-SI, Ni-R, and Ni-C/Ni-L constitute for the H_2 uptake reaction. In the active-ready oxidized state Ni-SI the cofactor reacts with CO or O_2 to form the inhibited species Ni-SCO or Ni-A/B, respectively.

Oxidation and deprotonation of Ni-R by one electron forms the Ni-C state [33]. The assignment of $\text{Ni}^{2+}/\text{Fe}^{2+}$ in Ni-R and $\text{Ni}^{3+}/\text{Fe}^{2+}$ in Ni-C is reflected by a CO frequency up-shift of up to $\sim 40\text{ cm}^{-1}$ for Ni-R3, compensated by the presence of a proton in Ni-R1 ($\sim 15\text{ cm}^{-1}$) and Ni-R2 ($\sim 30\text{ cm}^{-1}$) [20]. Both Ni-R and Ni-C carry a bridging hydride. The release of this hydride is accompanied by a two-fold reduction of the cofactor in the Ni-L states ($\text{Ni}^{1+}/\text{Fe}^{2+}$) and protonation of the protein fold [34,35]. Infrared data on Ni-L2 and Ni-L3 is rare; however, previous studies suggest a down-shift relative to Ni-C by $\sim 70\text{ cm}^{-1}$ and $\sim 85\text{ cm}^{-1}$, respectively [36–39]. This is compatible with a formal difference of two electrons. Oxidation and deprotonation restores Ni-SI and completes the cycle as shown in Figure 2. Whether Ni-L and/or Ni-C are included is subject to ongoing discussions [20,21].

Figure 2 additionally depicts the reaction of [NiFe]-hydrogenases with CO and O_2 . Carbon monoxide binds the terminal coordination site of Ni^{2+} in the Ni-SI state to form the oxidized, CO-inhibited Ni-SCO state [40]. This species differs from the parent Ni-SI state by a weakly coordinated Ni-CO ligand at high IR frequencies [41]. In the presence of O_2 , two different O_2 -inhibited, “super-oxidized” states may be enriched: Ni-A and Ni-B ($\text{Ni}^{3+}/\text{Fe}^{2+}$). Ni-A represents an “unready” species that converts slowly into Ni-SI while Ni-B is readily activated under reducing conditions [42,43]. [NiFe]-hydrogenases that do not form Ni-A maintain catalytic activity under aerobic conditions and have been classified O_2 -tolerant [14]. Standard [NiFe]-hydrogenases, e.g., as isolated from strict anaerobes are inhibited by O_2 and have been referred to as O_2 -sensitive [11]. Both Ni-A and Ni-B carry a Ni-Fe bridging ligand (most likely a hydroxo species) that reacts to H_2O upon reductive activation [44–46]. On structural level the kinetic activation differences between Ni-A and Ni-B remain elusive.

In this work we present the first conclusive IR characterization of the periplasmatic [NiFe]-hydrogenase HYD-2 from *E. coli*. In difference to HYD-1 [37], only tentative IR band assignments have been reported for HYD-2 [47,48]. We suggest an experimentally verified assignment of catalytic (Ni-SI, Ni-C, Ni-R) and inhibited states (Ni-SCO, Ni-B) making use of steady-state and real-time attenuated total reflection Fourier-transform infrared spectroscopy (ATR FTIR) under gas control. The reaction and mutual competition with H_2 , CO, and O_2 is probed in kinetic experiments and forms the basis for a comparative analysis with other [NiFe]-hydrogenases. Our methodology has mainly been applied to [FeFe]-hydrogenases in the past [49–51]. Here, we show that all advantages (low sample demand, simple experimental design, measurements under biological conditions, etc.) hold true for the analysis of [NiFe]-hydrogenases as well.

2. Results and Discussion

2.1. FTIR Steady-State and In Situ Difference Spectra

Synthesized and isolated in the absence of O₂, HYD-2 from *E. coli* adopted a steady-state mixture of at least two species (Figure 3a, first spectrum “as-isolated”). The carbonyl stretching frequencies are distinct enough ($\nu_{\text{CO}} = 1966$ and 1945 cm^{-1}) whereas the cyanide regime from $2100\text{--}2040 \text{ cm}^{-1}$ does not immediately suggest four individual ν_{CN^-} contributions. In the presence of 1% CO ambient partial pressure, the as-isolated spectrum completely converted into the oxidized, CO-inhibited state Ni-SCO (Figure 3a, second spectrum) [41]. This species is characterized by a high-frequency Ni-CO band ($\nu_{\text{CO}} = 2054 \text{ cm}^{-1}$) and a low-frequency Fe-CO band ($\nu_{\text{CO}} = 1944 \text{ cm}^{-1}$). The CN⁻ stretching frequencies can be found at 2084 and 2073 cm^{-1} . Isotope editing with ¹³CO confirmed the existence of two individual, vibrationally uncoupled CO ligands at the active site cofactor (Figure S1). When as-isolated HYD-2 was brought in contact with 1% O₂ (Figure 3a, third spectrum), an oxygen-inhibited state was populated ($\nu_{\text{CO}} = 1957 \text{ cm}^{-1}$ with $\nu_{\text{CN}^-} = 2092$ and 2082 cm^{-1}) that has been suggested to be Ni-B by Hexter and co-workers [47]. Incubation under 100% O₂ for up to four hours did not induce any further changes in the spectrum. In the presence of 1% H₂, ambient partial pressure the species observed in the as-isolated sample were found to be significantly diminished (Figure 3a, fourth spectrum). Even under 100% H₂, these states did not vanish completely (Figure S2). Three novel CO bands were detected at 1950 , 1936 , and 1927 cm^{-1} alongside a larger number of cyanide bands.

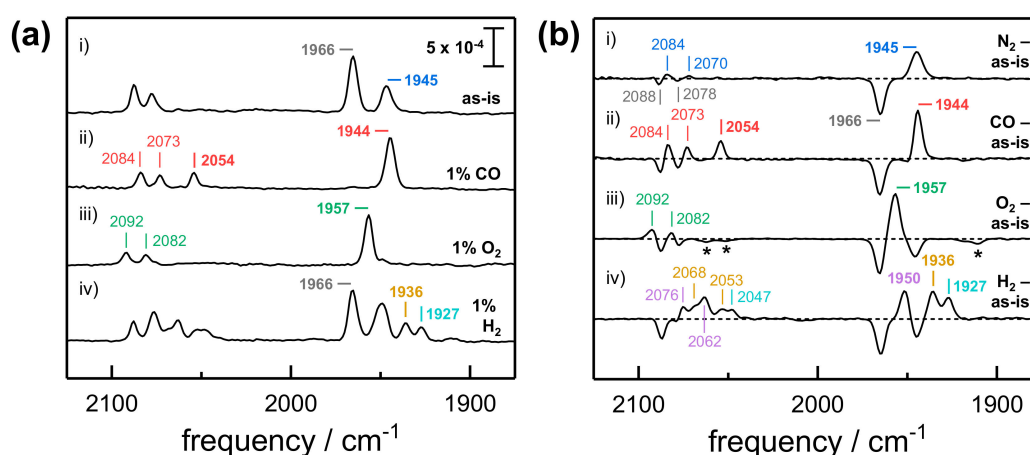


Figure 3. HYD-2 from *E. coli* in the presence of different gases. (a) Absorbance spectra under (i) N₂, (ii) CO, (iii) O₂, and (iv) H₂. All spectra are corrected for the broad contribution of liquid H₂O (see Appendix A). (b) Difference spectra. (i) Upon extensive treatment with N₂, the 1945 cm^{-1} species (CO marker band for Ni-SI) was enriched over the 1966 cm^{-1} species (Ni-C). (ii) The 1944 cm^{-1} species was populated to 100% under CO (Ni-SCO). (iii) The reaction with O₂ lead to a pure state as well (1957 cm^{-1} , CO marker band for Ni-B). (*) Note the decrease of a species at 1911 , 2062 , and 2052 cm^{-1} . (iv) The reduced species Ni-R1–R3 (1950 , 1936 , 1927 cm^{-1}) have been found to be enriched over Ni-C and Ni-SI in the presence of H₂.

In order to refine the band assignments, we recorded in situ difference spectra as a function of gas. For this an as-isolated absorbance spectrum was subtracted from the absorbance spectrum after the respective gas treatment (e.g., “H₂ – as-is”). The first spectrum in Figure 3b indicates a very slow enrichment of the 1945 cm^{-1} band over the 1966 cm^{-1} band upon elongated treatment with N₂ gas (the spectrum depicts a treatment with N₂ of more than four hours). This allows correlating CO and CN⁻ frequencies as suggested in the Figure 3b and Table 1. The enrichment under auto-oxidizing conditions (an inert gas is exploited to remove traces of evolved H₂ that otherwise would back-react with the enzyme [50]) indicates that the 1945 cm^{-1} band represents the active-ready,

oxidized state **Ni-SI**. This assignment is supported by the spectral similarity to **Ni-SCO** (Figure 3a) [41]. The concomitant decrease of the 1966 cm^{-1} band under oxidizing conditions suggests a reduced cofactor intermediate. According to the analyses of Ash et al. [20], the difference in CO stretching frequency of 21 cm^{-1} to **Ni-SI** strongly supports an assignment to the one-electron reduced hydride state **Ni-C**. Interestingly, the second spectrum in Figure 3b shows the loss of **Ni-SI** and **Ni-C** in the presence of CO although it is known that only **Ni-SI** is sensitive to CO inhibition [41]. Most likely, this reflects changes in the steady-state equilibrium between **Ni-C** and **Ni-SI** upon CO reacting with the later: once CO binds to the oxidized cofactor, reduced enzyme converts into **Ni-SI** and becomes reactive to CO. This process is related to intramolecular electron transfer and auto-oxidation of **Ni-C** into **Ni-SI** as discussed above, however much more effective because the CO affinity outrivals the H_2 release activity of HYD-2 [52], in particular under non-reducing conditions. Under O_2 , HYD-2 is oxidized into either **Ni-A** or **Ni-B** (Figure 3b, third spectrum). The difference spectrum shows a pronounced loss of **Ni-C** and **Ni-SI**, as well as a species at lower frequencies ($\nu\text{CO} = 1911\text{ cm}^{-1}$ with $\nu\text{CN}^- = 2062$ and 2052 cm^{-1}) that may represent an **Ni-L** state [34,35]. As HYD-2 is an O_2 -sensitive [NiFe]-hydrogenases, it is not immediately possible to conclude whether **Ni-A** or **Ni-B** was formed. In the presence of H_2 , the difference spectrum represents the enrichment of at least three novel species (Figure 3b, fourth spectrum). The corresponding three CO bands are clearly visible in the difference spectrum, and the downshift relative to **Ni-C** suggests an assignment of **Ni-R1** (1950 cm^{-1}), **Ni-R2** (1936 cm^{-1}), and **Ni-R3** (1927 cm^{-1}) [32]. In Figure S2, the correlation of CO and CN^- bands for the R-states is presented.

Table 1. Experimentally identified redox species. All frequencies given in cm^{-1} .

Species	νCO	νCN^-	νCN^-
Ni-B	1957	2082	2092
Ni-SI	1945	2070	2084
Ni-SCO ¹	2054/1944	2073	2084
Ni-C	1966	2078	2088
Ni-R1	1950	2062	2076
Ni-R2	1936	2053	2068
Ni-R3	1929	2047	2063
Ni-L	1911	2052	2062

¹ In the presence of ^{13}CO the Ni-CO band shifts to 2009 cm^{-1} .

2.2. Kinetic Traces for the Reaction with H_2 , CO, and O_2

Figure 4 illustrates the reaction of HYD-2 to changes of the N_2/H_2 gas composition in the head phase above the protein film. The sum of peak area of one CO and two CN^- bands for each species is followed over time. In as-isolated sample, **Ni-C** and **Ni-SI** were populated in a ratio of approximately 2:1. When the inert N_2 atmosphere was enriched with 1% H_2 ambient partial pressure a steep decrease of both these species was observed; however, while **Ni-SI** vanished from the spectrum completely **Ni-C** lost only ~40% sum of peak area and remained to be the most prominent species. **Ni-R1** rose in the presence of H_2 over **Ni-SI** and **Ni-C** as dominant “super-reduced” state while **Ni-R2** and **Ni-R3** are omitted for clarity (see Figure S2 for the complete data set). Removal of H_2 resulted in a slow conversion of the R-states back into **Ni-C** and **Ni-SI**, compared to the fast decrease under H_2 . **Ni-SI** only reaches ~50% sum of peak area in comparison to as-isolated sample. No traces of **Ni-A**, **Ni-B**, or **Ni-SCO** were observed.

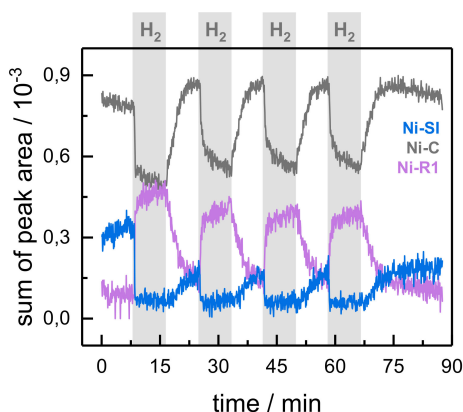


Figure 4. Repeated N_2/H_2 cycles on HYD-2 from *E. coli*. The sum of peak area of CO/ CN^- bands assigned to each state is plotted against time. In the presence of 1% H_2 ambient partial pressure, Ni-C and Ni-SI are diminished in favor of the “super-reduced” R-states. The one-electron reduced hydride state Ni-C (black) is the dominating species throughout the experiment. The experiment demonstrates the robust nature of the Ni-C/Ni-SI \leftrightarrow Ni-R1 conversion.

Figure 5 depicts on the inhibition and reactivation kinetics upon contact with CO in either N_2 or H_2 carrier gas. Panel (a) shows how Ni-C and Ni-SI were populated under N_2 and converted into Ni-SCO at 1% CO. After 500 s, CO was removed from the gas phase, which prompted the film to swing into an equilibrium between Ni-SCO and Ni-SI. The CO-inhibited species remained to be the dominant, though. After 500 s, 1% H_2 was introduced to the gas stream and gave rise to Ni-C/Ni-R over Ni-SCO/Ni-SI. The reaction of CO with the reduced active site cofactor is addressed in Figure 5b. Here, the percentage of CO was stepped up systematically in H_2 carrier gas. Half-max intensity for Ni-SCO is achieved at $\sim 30\%$ CO (Figure S3), whereas only 1% CO resulted in a full conversion under N_2 (Figure 5a). The observed decline of reduced states cannot be explained by the relative decrease of H_2 ambient partial pressure between 100 and 50%: Figure 4 and Figure S2 showed that 1% H_2 is sufficient for a reduction of HYD-2, therefore no significant changes in the effective H_2 redox potential can be assumed. Similar to the equilibrium between Ni-C and Ni-SI (see above) the R-states are in equilibrium with the “unprotected” Ni-SI state under reducing conditions (Figure 5b). In the presence of CO Ni-SI reacts to Ni-SCO, which induces a continuous auto-oxidation of the reduced species into Ni-SI (note the relative stable population of Ni-SI up to 10% CO). The enrichment of Ni-C and Ni-R under H_2 affects this equilibrium and delays the process of auto-oxidation. This results in an indirect protection against CO inhibition although H_2 and CO do not compete for the same binding site (compare Figure 2) [40]. No reaction with CO is observed in the absence of Ni-SI, i.e., under O_2 (Figure S3).

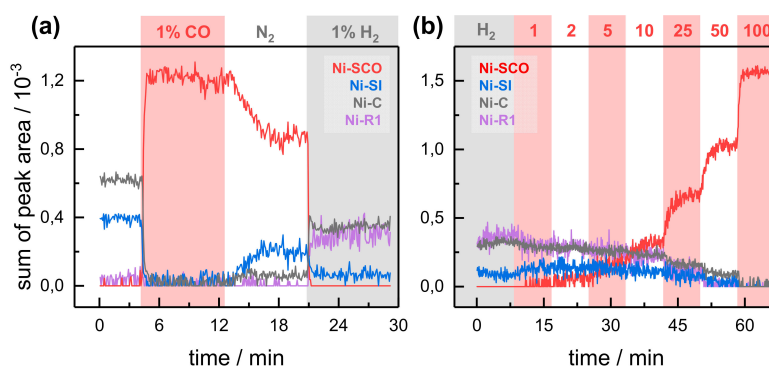


Figure 5. Inhibition of HYD-2 from *E. coli* with CO in either N_2 or H_2 carrier gas. (a) With 1% CO in N_2 carrier gas HYD-2 converts into Ni-SCO immediately (red trace). The species was semi-stable in the absence of CO (100% N_2) adopting an equilibrium with Ni-SI (blue trace). Under 1% H_2 an immediate conversion into the catalytic species Ni-C and Ni-R was observed. (b) In contrast, using H_2 as carrier gas it takes significantly higher concentrations of CO to convert the enzyme into Ni-SCO.

In a similar set of experiments, Figure 6 depicts on the inhibition and reactivation kinetics of HYD-2 upon contact with O₂ in the presence of either N₂ or H₂ carrier gas. Under 1% O₂, Ni-C and Ni-SI were converted into a single species, i.e., Ni-A or Ni-B (Figure 6a, N₂ carrier gas). In difference to the reaction with CO, no changes in equilibrium were observed upon removal of O₂ from the gas stream and the oxygen-inhibited species remained stable even in the absence of O₂. After 500 s, 1% H₂ was introduced to the gas stream, resulting in a conversion of the oxygen-inhibited species into the typical mixture of Ni-C and Ni-R as seen before (Figure 4). Based on the apparent reactivity of the oxygen-inhibited species, we propose to assign the identified IR signature under O₂ to Ni-B, in agreement with earlier suggestions [47]. HYD-2 was stable under 100% O₂ for at least four hours with no notable decrease or conversion into any other species, e.g., Ni-A.

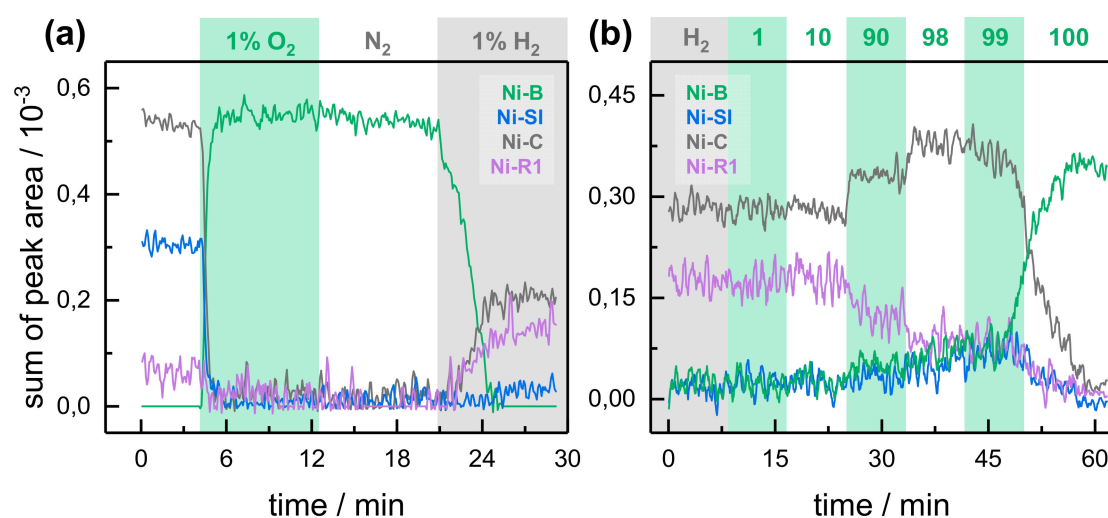


Figure 6. Inhibition of HYD-2 from *E. coli* with O₂ in either N₂ or H₂ carrier gas. (a) With 1% CO in N₂ carrier gas HYD-2 converts into Ni-B immediately (green trace). Ni-B is stable under 100% N₂ and converted in the presence of 1% H₂ into reduced species Ni-C/Ni-R within minutes. (b) The mutual robustness of the hydride-binding species Ni-C and Ni-R shows in the right panel as well: Ni-B is enriched in the film only at 99–100% O₂. Potentially explosive mixtures of 15–85% O₂ in H₂ were avoided.

In the next step, HYD-2 was subjected to increasing concentration of O₂ in the presence of H₂ carrier gas (Figure 6b). The system did not convert into Ni-B until 99–100% O₂ was reached. In difference to the reaction with CO, the lack of O₂ inhibition under reducing conditions can be explained by competition of O₂ and H₂ for the same binding site at the [NiFe] cofactor [40,53]. Interestingly, Ni-C is populated over Ni-R from 90–98% O₂, most likely reflecting the instability of the “super-reduced” R-states under increasingly oxidizing conditions. This hints at an equilibrium between hydrogenase- and oxygenase-activity that has been suggested to explain the hydrogen turnover activity of “O₂-tolerant” [NiFe]-hydrogenases [54]. Accordingly, the diverging reaction kinetics from CO- and O₂ inhibition as highlighted in Figure 7 may indicate the difference between CO release (fast) and O₂ reduction (slow).

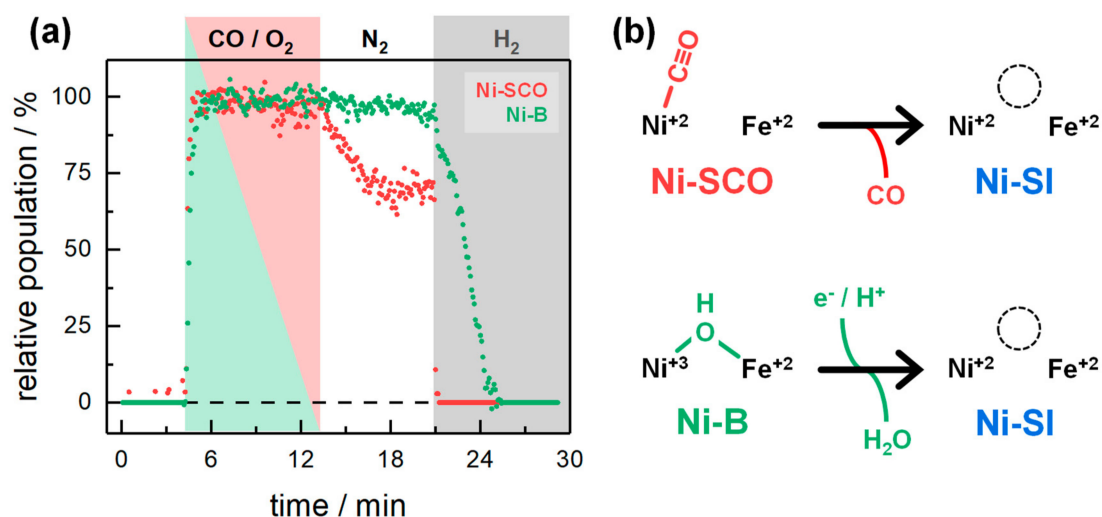


Figure 7. (a) Direct comparison of the reaction with CO (Ni-SCO, red trace) and O₂ (Ni-B, green trace). Introduction of either 1% CO or O₂ to the N₂ gas stream resulted in a fast and complete conversion into Ni-SCO or Ni-B, respectively. Under 100% N₂, the CO-inhibited state is semi-stable whereas no decrease of Ni-B was observed. Ni-SCO was immediately lost in the presence of 1% H₂ whereas the reductive activation of Ni-B took significantly longer. (b) While CO binds to Ni-SI with no changes in the electronic structure of the [NiFe] cofactor (top) [41], O₂ oxidizes the active site and forms a Ni-Fe bridging hydroxo ligand (bottom) [44–46]. Reactivation from O₂ inhibition may include proton-coupled electron transport and the release of water [16]. This is reflected in the pronounced difference in activation time under 1% H₂ (left panel). Note that reductive reactivation of Ni-B comprises additional species most likely. Furthermore, Ni-SI is a transient intermediate in the reaction with H₂.

3. Materials and Methods

3.1. Synthesis and Isolation of HYD-2 from *E. coli*

To synthesize and isolate preparative amounts of active [NiFe]-hydrogenase, 5 mL “reaction mix” were used. As reported earlier [48], this mixture contained StrepHybC (HYD-2 catalytic subunit) and the purified maturases HybG-HybDE (GDE complex) and HypEF. An “activation mix” comprising ATP, carbamoylphosphate, NiCl₂, FeSO₄, and sodium dithionite was added. After incubation at room temperature in the absence of air, cofactor synthesis was initiated adding endopeptidase HybD. After 30 min, the mixture was supplemented with HYD-2 subunit HisHybO. Active StrepHybC-HisHybO heterocomplex (HYD-2 holoenzyme) was isolated from the reaction mix by strep-tactin affinity chromatography and histidine affinity chromatography. The sample was concentrated to ~200 μM protein concentration in 100 mM Tris/HCl buffer (pH 8) including 1 mM dodecyl maltoside as detergent. See ref. [48,55] for further details.

3.2. Infrared Spectroscopy

All spectroscopy was performed at room temperature and in the dark on a Bruker Tensor27 FTIR spectrometer (Ettlingen, Germany) housed in a CoyLab anaerobic chamber. A DuraSamplIR 2 optical cell with a three-reflections silicon microcrystal was used for ATR spectroscopy. Beam path, spectrometer, and anaerobic chamber were purged with dry N₂ gas as provided by an Inmatec (Hersching, Germany) nitrogen generator (gas purity 5.0). For each experiment, 1 μL of HYD-2 protein sample (~200 μM) was pipetted onto the silicon crystal, dried under N₂, and rehydrated in the presence of an aerosol by running the gas mixture through a wash bottle with a buffer solution of 10 mM Tris/HCl (pH 8). Digital mass flow controllers (Sierra Instruments, Monterey, CA, USA) were used to adjust the absolute amount of gas and ratio between reactants. All gas treatments were

performed at ambient partial pressure (1.013 bar). Following this procedure, concentrated and stable protein films were formed (Figure A1). See ref. [50] for details of the experimental setup.

Data were recorded with a spectral resolution of 2 cm^{-1} (80 kHz scanner velocity) and 1.000 interferometer scans (steady-state spectra) or 25 scans in time-resolved experiments. Difference spectra were calculated from single channel spectra via OPUS software. In order to analyze spectral changes in the cofactor regime from $2150\text{--}1850\text{ cm}^{-1}$, absorbance spectra were corrected for the background contribution of liquid water by a low frequency spline function using a home-written routine. The CO/CN⁻ signature of all redox species was trained on pure spectra to evaluate the individual frequencies, peak areas, and peak ratios. The “sum of peak area” as obtained by Gaussian fits was plotted to follow the conversion of species over time. In Figure A2, this procedure is demonstrated on a representative data set.

4. Conclusions

The membrane-associated, bidirectional [NiFe]-hydrogenase HYD-2 from *E. coli* has been analyzed by in situ ATR FTIR spectroscopy. Based on the reactivity with H₂, CO, and O₂, an experimental band assignment is suggested that agrees well with other [NiFe]-hydrogenases (Table 1). In contrast to HYD-1 from *E. coli*, the one-electron reduced Ni-L states were barely observed and the formally isoelectronic hydride state Ni-C represents the most stable redox species. This suggests superior stabilization of the Ni-Fe bridging hydride in HYD-2 and may be related to the diverging catalytic properties of HYD-1 (H₂ uptake) and HYD-2 (bidirectional) [52]. In the future, we will explore the differences between Hyd-1 and Hyd-2, making use of the unique possibilities of in vitro maturation (e.g., site-specific isotope editing or Hyd-1/Hyd-2 hybrid constructs) [48].

We have no reason to conclude that anything other than Ni-B was enriched in the presence of O₂. Ni-A and Ni-B are difficult to distinguish by IR spectroscopy. However, in comparison to the O₂-sensitive hydrogenases of strict anaerobes that recover from O₂ inhibition over the time course of hours, the spectral assignment to Ni-B is easily compatible with the fast reactivation kinetics of HYD-2 observed in our experiments. The crystal structure of HYD-2 clearly indicates a standard [4Fe-4S] cluster proximal to the [NiFe] cofactor, well in agreement with protein film electrochemistry on HYD-2 that prompted a classification as O₂-sensitive. Thus, HYD-2 was expected to show low rates of reductive reactivation and to form Ni-A upon reacting with O₂. This is not the case. With respect to O₂ tolerance, the role of the proximal iron-sulfur cluster in the membrane-bound [NiFe] hydrogenase of *Ralstonia eutropha* has been questioned recently [56]. The example of HYD-2 from *E. coli* shows that the reaction with O₂ may involve additional check screws like proton- and electron transfer that remain to be evaluated.

Supplementary Materials: The following are available online at <http://www.mdpi.com/2073-4344/8/11/530/s1>, Figure S1: ¹³CO isotope editing, Figure S2: Further H₂ titrations and Ni-R band assignment, Figure S3: Further CO titrations.

Author Contributions: Conceptualization, S.T.S. and M.S.; methodology, S.T.S. and M.S.; formal analysis, S.T.S.; investigation, M.S. and K.L.; resources, B.S.; supervision, S.T.S.

Funding: Basem Soboh acknowledges funding by the DFG priority program “FeS for life” (SPP-1927).

Conflicts of Interest: The authors declare no conflict of interest.

Appendix A

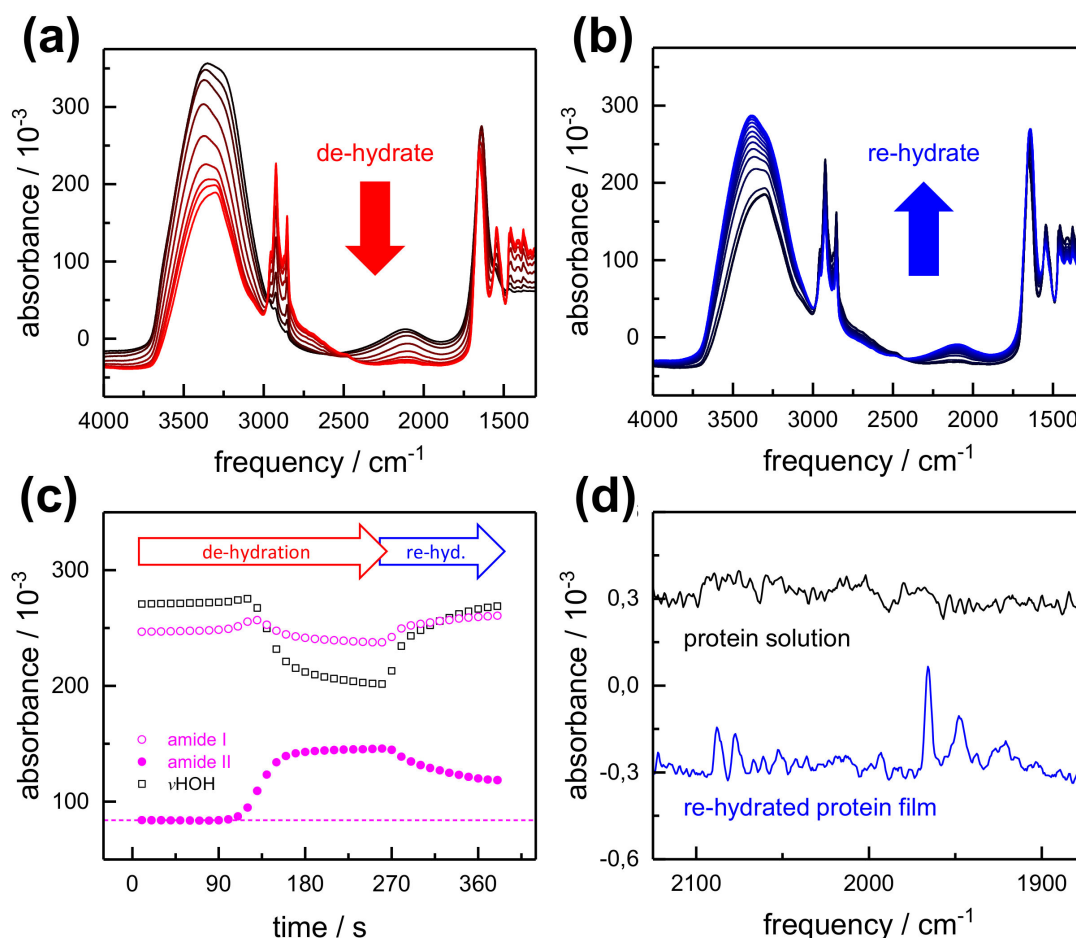


Figure A1. Preparation of the protein film. (a) protein solution (1 μL) of $\sim 200 \mu\text{M}$ HYD-2 was pipetted to the ATR crystal and carefully “de-hydrated” under dry N_2 . The spectra in the graph run from black (protein solution) to red (protein film). (b) Humidification of carrier N_2 induces a “re-hydration” of the protein film. This is an important prerequisite to follow the specific reactivity of HYD-2 to varying gases. The spectra in the graph run from black (dry protein film) to blue (re-hydrated film). (c) Due to the overlap of water and protein bands, the changes in the film are not trivial to analyze. In particular, following the amide I band ($\sim 1655 \text{ cm}^{-1}$, open circles) and HOH bending mode intensity ($\sim 1635 \text{ cm}^{-1}$, open squares) is not helpful. The amide II band (1540 cm^{-1} , full circles) shares less overlap with liquid water and can be addressed to follow the changes in protein concentration more reliably. Upon de-hydration the band intensity increases by $\sim 60 \times 10^{-3}$ absorbance units while the decrease upon re-hydration accounts to only $\sim 20 \times 10^{-3}$ absorbance units. For a comparable hydration level, we observe a $\sim 40 \times 10^{-1}$ net-increase of amide II band intensity. (d) In the cofactor regime, the CO/CN^- become visible in the re-hydrated film (blue spectrum) where no such bands are observed with protein solution (black spectrum). Both spectra are baseline-corrected (see Figure A2). The inferior signal-to-noise level in comparison to Figure 3a stems from the number of averages (here: 50 interferometer scans).

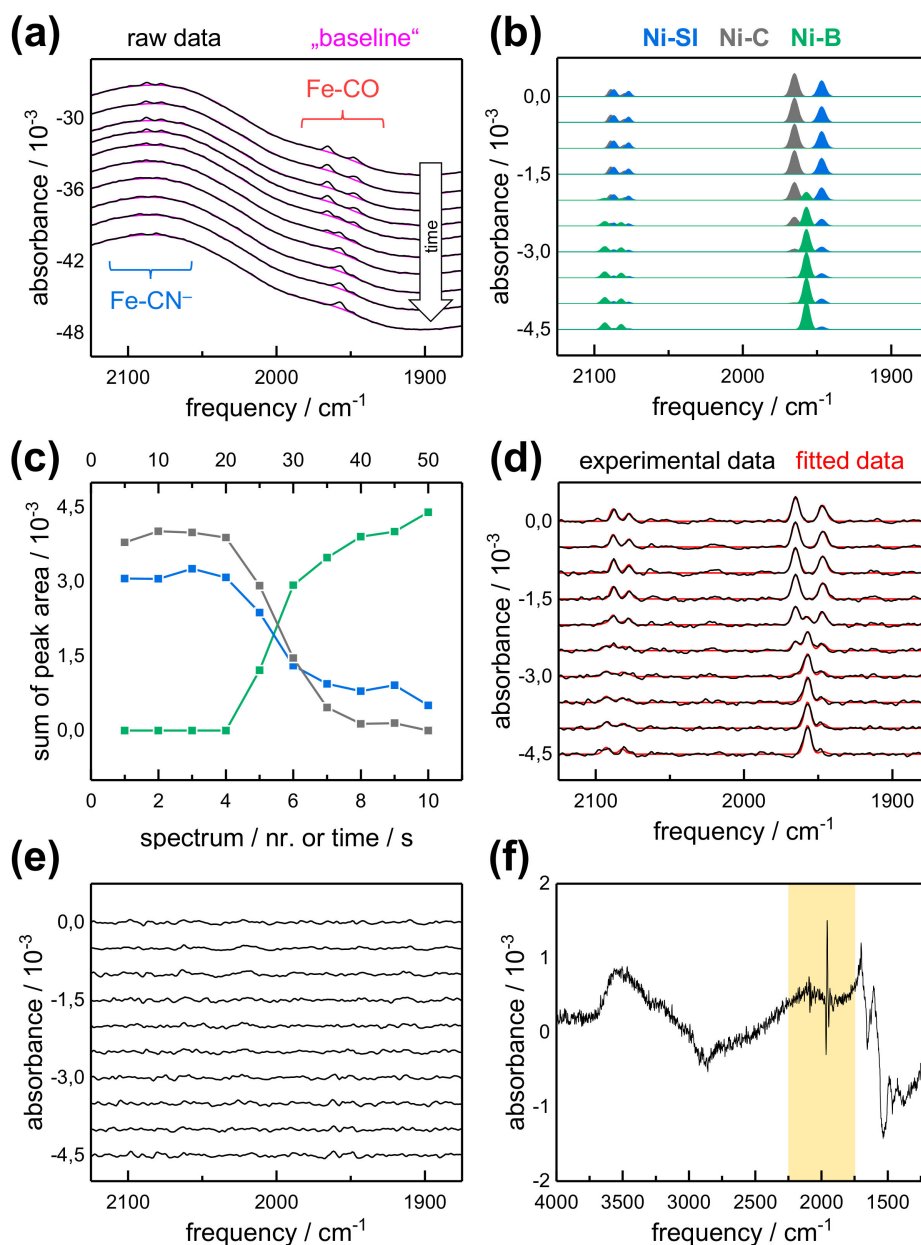


Figure A2. Baseline correction, data fitting, kinetic description, and quality assurance at the example of the formation of Ni-B in the presence of O₂. All spectra are plotted from “as-isolated” (top) to “O₂-inhibited” (bottom). (a) Absorbance spectra (raw data, black) were corrected for the broad contribution of liquid water by spline functions (magenta). The CO- and CN⁻ regime is indicated. (b) The Fe(CN)₂CO signature of the cofactor is described by three Gaussian fits including frequency, peak area, and peak ratio for each redox species. This data was obtained from pure spectra for Ni-SI (blue), Ni-C (black), and Ni-B (green) beforehand. (c) The “sum of peak area” (CO + CN + CN) for each species is then plotted over the number of spectra. Depending on scanner velocity (80 kHz), spectral resolution (2 cm⁻¹), and number of averages (e.g., 25 interferometer scans), this value is converted into time. (d) Overlay of baseline-subtracted data (black) and fitted trace (envelope, red). (e) The residuals (“data – fit”) do not suggest any additional species and allow estimating the signal-to-noise ratio. (f) A difference spectrum between the last and first spectrum indicates a small increase of water (OH stretching, ~3500 cm⁻¹) that is accompanied by a decrease of protein signals (amide I, ~1655 cm⁻¹ and amide II, ~1540 cm⁻¹). These unspecific changes do not significantly affect the cofactor regime from 2150–1850 cm⁻¹ (yellow mark-up).

References

1. Lubitz, W.; Ogata, H.; Ru, O.; Reijerse, E. Hydrogenases. *Chem. Rev.* **2014**, *114*, 4081–4148. [[CrossRef](#)] [[PubMed](#)]
2. Shima, S.; Thauer, R.K. A third type of hydrogenase catalyzing H₂ activation. *Chem. Rec.* **2007**, *7*, 37–46. [[CrossRef](#)] [[PubMed](#)]
3. Ogata, H.; Lubitz, W.; Higuchi, Y. Structure and function of [NiFe] hydrogenases. *J. Biochem.* **2016**, *160*, 251–258. [[CrossRef](#)] [[PubMed](#)]
4. Stripp, S.T.; Happe, T. How Algae Produce Hydrogen—News from the Photosynthetic Hydrogenase. *Dalton Trans.* **2009**, *45*, 9960–9969. [[CrossRef](#)] [[PubMed](#)]
5. Vignais, P.M.; Billoud, B. Occurrence, classification, and biological function of hydrogenases: An overview. *Chem. Rev.* **2007**, *107*, 4206–4272. [[CrossRef](#)] [[PubMed](#)]
6. Tard, C.; Pickett, C.J. Structural and functional analogues of the active sites of the [Fe]-, [NiFe]-, and [FeFe]-hydrogenases. *Chem. Rev.* **2009**, *109*, 2245–2274. [[CrossRef](#)] [[PubMed](#)]
7. Simmons, T.R.; Berggren, G.; Bacchi, M.; Fontecave, M.; Artero, V. Mimicking hydrogenases: From biomimetics to artificial enzymes. *Coord. Chem. Rev.* **2014**, *270–271*, 127–150. [[CrossRef](#)]
8. Schilter, D.; Camara, J.M.; Huynh, M.T.; Hammes-Schiffer, S.; Rauchfuss, T.B. Hydrogenase Enzymes and Their Synthetic Models: The Role of Metal Hydrides. *Chem. Rev.* **2016**, *116*, 8693–8749. [[CrossRef](#)] [[PubMed](#)]
9. Sargent, F. *The Model [NiFe]-Hydrogenases of Escherichia coli*, 1st ed.; Elsevier Ltd.: Amsterdam, The Netherlands, 2016; Volume 68, ISBN 9780128048238.
10. Laurinavichene, T.V.; Tsygankov, A.A. H₂ consumption by *Escherichia coli* coupled via hydrogenase 1 or hydrogenase 2 to different terminal electron acceptors. *FEMS Microbiol. Lett.* **2001**, *202*, 121–124. [[CrossRef](#)] [[PubMed](#)]
11. Vincent, K.A.; Parkin, A.; Lenz, O.; Albracht, S.P.J.; Fontecilla-Camps, J.C.; Cammack, R.; Friedrich, B.; Armstrong, F.A. Electrochemical definitions of O₂ sensitivity and oxidative inactivation in hydrogenases. *J. Am. Chem. Soc.* **2005**, *127*, 18179–18189. [[CrossRef](#)] [[PubMed](#)]
12. Lukey, M.J.; Roessler, M.M.; Parkin, A.; Evans, R.M.; Davies, R.A.; Lenz, O.; Friedrich, B.; Sargent, F.; Armstrong, F.A. Oxygen-Tolerant [NiFe]-Hydrogenases: The Individual and Collective Importance of Supernumerary Cysteines at the Proximal Fe-S Cluster. *J. Am. Chem. Soc.* **2011**, *133*, 16881–16892. [[CrossRef](#)] [[PubMed](#)]
13. Beaton, S.E.; Evans, R.M.; Finney, A.J.; Lamont, C.M.; Armstrong, F.A.; Sargent, F.; Carr, S.B. The Structure of Hydrogenase-2 from *Escherichia coli*: Implications for H₂-Driven Proton Pumping. *Biochem. J.* **2018**, *2*, BCJ20180053. [[CrossRef](#)] [[PubMed](#)]
14. Fritsch, J.; Lenz, O.; Friedrich, B. Structure, function and biosynthesis of O₂-tolerant hydrogenases. *Nat. Rev.* **2013**, *11*, 106–114. [[CrossRef](#)] [[PubMed](#)]
15. Fritsch, J.; Scheerer, P.; Frielingsdorf, S.; Kroschinsky, S.; Friedrich, B.; Lenz, O.; Spahn, C.M.T. The crystal structure of an oxygen-tolerant hydrogenase uncovers a novel iron-sulphur centre. *Nature* **2011**, *479*, 249–252. [[CrossRef](#)] [[PubMed](#)]
16. Qiu, S.; Olsen, S.; MacFarlane, D.R.; Sun, C. The oxygen reduction reaction on [NiFe] hydrogenases. *Phys. Chem. Chem. Phys.* **2018**, *20*, 23528–23534. [[CrossRef](#)] [[PubMed](#)]
17. Volbeda, A.; Amara, P.; Darnault, C.; Mouesca, J.-M.; Parkin, A.; Roessler, M.M.; Armstrong, F.A.; Fontecilla-Camps, J.C. X-ray crystallographic and computational studies of the O₂-tolerant [NiFe]-hydrogenase 1 from *Escherichia coli*. *Proc. Natl. Acad. Sci. USA* **2012**, *109*, 5305–5310. [[CrossRef](#)] [[PubMed](#)]
18. Volbeda, A.; Darnault, C.; Parkin, A.; Sargent, F.; Armstrong, F.A.; Fontecilla-Camps, J.C. Crystal structure of the O₂-tolerant membrane-bound hydrogenase 1 from *Escherichia coli* in complex with its cognate cytochrome *b*. *Structure* **2013**, *21*, 184–190. [[CrossRef](#)] [[PubMed](#)]
19. Pierik, A.J.; Roseboom, W.; Happe, R.P.; Bagley, K.A.; Albracht, S.P.J. Carbon monoxide and cyanide as intrinsic ligands to iron in the active site of [NiFe]-hydrogenases. *J. Biol. Chem.* **1999**, *274*, 3331–3337. [[CrossRef](#)] [[PubMed](#)]
20. Ash, P.A.; Hidalgo, R.; Vincent, K.A. Proton Transfer in the Catalytic Cycle of [NiFe] Hydrogenases: Insight from Vibrational Spectroscopy. *ACS Catal.* **2017**, *7*, 2471–2485. [[CrossRef](#)] [[PubMed](#)]
21. Tai, H.; Higuchi, Y.; Hirota, S. Comprehensive reaction mechanisms at and near the Ni-Fe active sites of [NiFe] hydrogenases. *Dalton Trans.* **2018**, *47*, 4408–4423. [[CrossRef](#)] [[PubMed](#)]

22. Pandelia, M.-E.; Ogata, H.; Lubitz, W. Intermediates in the catalytic cycle of [NiFe] hydrogenase: Functional spectroscopy of the active site. *ChemPhysChem* **2010**, *11*, 1127–1140. [[CrossRef](#)] [[PubMed](#)]
23. De Lacey, A.L.; Pardo, A.; Fernández, V.M.; Dementin, S.; Adryanczyk-Perrier, G.; Hatchikian, E.; Rousset, M. FTIR spectroelectrochemical study of the activation and inactivation processes of [NiFe] hydrogenases: Effects of solvent isotope replacement and site-directed mutagenesis. *J. Biol. Chem.* **2004**, *9*, 636–642. [[CrossRef](#)] [[PubMed](#)]
24. Greene, B.L.; Wu, C.; Vansuch, G.E.; Adams, M.W.W.; Dyer, R.B. Proton Inventory and Dynamics in the Ni_a-S to Ni_a-C Transition of a [NiFe] Hydrogenase. *Biochemistry* **2016**, *55*, 1813–1825. [[CrossRef](#)] [[PubMed](#)]
25. Ogata, H.; Nishikawa, K.; Lubitz, W. Hydrogens detected by subatomic resolution protein crystallography in a [NiFe] hydrogenase. *Nature* **2015**, *520*, 571–574. [[CrossRef](#)] [[PubMed](#)]
26. Evans, R.M.; Brooke, E.J.; Wehlin, S.A.M.; Nomerotskaia, E.; Sargent, F.; Carr, S.B.; Phillips, S.E.V.; Armstrong, F.A. Mechanism of hydrogen activation by [NiFe] hydrogenases. *Nat. Chem. Biol.* **2016**, *12*, 46–50. [[CrossRef](#)] [[PubMed](#)]
27. Lubitz, W.; Reijerse, E.; van Gastel, M. [NiFe] and [FeFe] hydrogenases studied by advanced magnetic resonance techniques. *Chem. Rev.* **2007**, *107*, 4331–4365. [[CrossRef](#)] [[PubMed](#)]
28. Vincent, K.A.; Parkin, A.; Armstrong, F.A. Investigating and exploiting the electrocatalytic properties of hydrogenases. *Chem. Rev.* **2007**, *107*, 4366–4413. [[CrossRef](#)] [[PubMed](#)]
29. Fontecilla-Camps, J.C.; Volbeda, A.; Cavazza, C.; Nicolet, Y. Structure/function relationships of [NiFe]- and [FeFe]-hydrogenases. *Chem. Rev.* **2007**, *107*, 4273–4303. [[CrossRef](#)] [[PubMed](#)]
30. Van der Spek, T.M.; Arendsen, A.F.; Happe, R.P.; Yun, S.; Bagley, K.A.; Stufkens, D.J.; Hagen, W.R.; Albracht, S.P. Similarities in the architecture of the active sites of Ni-hydrogenases and Fe-hydrogenases detected by means of infrared spectroscopy. *Eur. J. Biochem.* **1996**, *237*, 629–634. [[CrossRef](#)] [[PubMed](#)]
31. Brecht, M.; Van Gastel, M.; Buhrke, T.; Friedrich, B.; Lubitz, W. Direct Detection of a Hydrogen Ligand in the [NiFe] Center of the Regulatory H₂-Sensing Hydrogenase from *Ralstonia eutropha* in Its Reduced State by HYSCORE and ENDOR Spectroscopy. *J. Am. Chem. Soc.* **2003**, *125*, 13075–13083. [[CrossRef](#)] [[PubMed](#)]
32. De Lacey, A.L.; Fernandez, V.M.; Rousset, M.; Cammack, R. Activation and inactivation of hydrogenase function and the catalytic cycle: Spectroelectrochemical studies. *Chem. Rev.* **2007**, *107*, 4304–4330. [[CrossRef](#)] [[PubMed](#)]
33. Albracht, S.P.J. Nickel hydrogenases: In search of the active site. *BBA Bioenerg.* **1994**, *1188*, 167–204. [[CrossRef](#)]
34. Fichtner, C.; van Gastel, M.; Lubitz, W. Wavelength dependence of the photo-induced conversion of the Ni-C to the Ni-L redox state in the [NiFe] hydrogenase of *Desulfovibrio vulgaris* Miyazaki F. *Phys. Chem. Chem. Phys.* **2003**, *5*, 5507–5513. [[CrossRef](#)]
35. Schröder, O.; Bleijlevens, B.; De Jongh, T.E.; Chen, Z.; Li, T.; Fischer, J.; Förster, J.; Friedrich, C.G.; Bagley, K.A.; Albracht, S.P.J.; et al. Characterization of a cyanobacterial-like uptake [NiFe] hydrogenase: EPR and FTIR spectroscopic studies of the enzyme from *Acidithiobacillus ferrooxidans*. *J. Biol. Inorg. Chem.* **2007**, *12*, 212–233. [[CrossRef](#)] [[PubMed](#)]
36. Pandelia, M.E.; Infossi, P.; Stein, M.; Giudici-Orticoni, M.T.; Lubitz, W. Spectroscopic characterization of the key catalytic intermediate Ni-C in the O₂-tolerant [NiFe] hydrogenase i from *Aquifex aeolicus*: Evidence of a weakly bound hydride. *Chem. Commun.* **2012**, *48*, 823–825. [[CrossRef](#)] [[PubMed](#)]
37. Hidalgo, R.; Ash, P.A.; Healy, A.J.; Vincent, K.A. Infrared spectroscopy during electrocatalytic turnover reveals the Ni-L active site state during H₂ oxidation by a NiFe hydrogenase. *Angew. Chem. Int. Ed.* **2015**, *54*, 7110–7113. [[CrossRef](#)] [[PubMed](#)]
38. Murphy, B.J.; Hidalgo, R.; Roessler, M.M.; Evans, R.M.; Ash, P.A.; Myers, W.K.; Vincent, K.A.; Armstrong, F.A. Discovery of Dark pH-Dependent H⁺ Migration in a [NiFe]-Hydrogenase and Its Mechanistic Relevance: Mobilizing the Hydrido Ligand of the Ni-C Intermediate. *J. Am. Chem. Soc.* **2015**, *137*, 8484–8489. [[CrossRef](#)] [[PubMed](#)]
39. Tai, H.; Nishikawa, K.; Inoue, S.; Higuchi, Y.; Hirota, S. FT-IR Characterization of the Light-Induced Ni-L2 and Ni-L3 States of [NiFe] Hydrogenase from *Desulfovibrio vulgaris* Miyazaki F. *J. Phys. Chem. B* **2015**, 150430101225004. [[CrossRef](#)] [[PubMed](#)]

40. Ogata, H.; Mizoguchi, Y.; Mizuno, N.; Miki, K.; Adachi, S.; Yasuoka, N.; Yagi, T.; Yamauchi, O.; Hirota, S.; Higuchi, Y. Structural studies of the carbon monoxide complex of [NiFe]hydrogenase from *Desulfovibrio vulgaris* Miyazaki F: Suggestion for the initial activation site for dihydrogen. *J. Am. Chem. Soc.* **2002**, *124*, 11628–11635. [[CrossRef](#)] [[PubMed](#)]
41. Pandelia, M.E.; Ogata, H.; Currell, L.J.; Flores, M.; Lubitz, W. Inhibition of the [NiFe] hydrogenase from *Desulfovibrio vulgaris* Miyazaki F by carbon monoxide: An FTIR and EPR spectroscopic study. *Biochim. Biophys. Acta Bioenerg.* **2010**, *1797*, 304–313. [[CrossRef](#)] [[PubMed](#)]
42. Lamle, S.E.; Albracht, S.P.J.; Armstrong, F.A. Electrochemical potential-step investigations of the aerobic interconversions of [NiFe]-hydrogenase from *Allochromatium vinosum*: Insights into the puzzling difference between unready and ready oxidized inactive states. *J. Am. Chem. Soc.* **2004**, *126*, 14899–14909. [[CrossRef](#)] [[PubMed](#)]
43. Bleijlevens, B.; van Broekhuizen, F.A.; De Lacey, A.L.; Roseboom, W.; Fernandez, V.M.; Albracht, S.P.J. The activation of the [NiFe]-hydrogenase from *Allochromatium vinosum*. An infrared spectro-electrochemical study. *J. Biol. Inorg. Chem.* **2004**, *9*, 743–752. [[CrossRef](#)] [[PubMed](#)]
44. Volbeda, A.; Martin, L.; Cavazza, C.; Matho, M.; Faber, B.W.; Roseboom, W.; Albracht, S.P.J.; Garcin, E.; Rousset, M.; Fontecilla-Camps, J.C. Structural differences between the ready and unready oxidized states of [NiFe] hydrogenases. *J. Biol. Inorg. Chem.* **2005**, *10*, 239–249. [[CrossRef](#)] [[PubMed](#)]
45. Ogata, H.; Hirota, S.; Nakahara, A.; Komori, H.; Shibata, N.; Kato, T.; Kano, K.; Higuchi, Y. Activation process of [NiFe] hydrogenase elucidated by high-resolution X-ray analyses: Conversion of the ready to the unready state. *Structure* **2005**, *13*, 1635–1642. [[CrossRef](#)] [[PubMed](#)]
46. Barilone, J.L.; Ogata, H.; Lubitz, W.; Van Gastel, M. Structural differences between the active sites of the Ni-A and Ni-B states of the [NiFe] hydrogenase: An approach by quantum chemistry and single crystal ENDOR spectroscopy. *Phys. Chem. Chem. Phys.* **2015**, *17*, 16204–16212. [[CrossRef](#)] [[PubMed](#)]
47. Hexter, S.V.; Chung, M.-W.; Vincent, K.A.; Armstrong, F.A. Unusual Reaction of [NiFe]-Hydrogenases with Cyanide. *J. Am. Chem. Soc.* **2014**, *136*, 10470–10477. [[CrossRef](#)] [[PubMed](#)]
48. Senger, M.; Stripp, S.T.; Soboh, B. Proteolytic cleavage orchestrates cofactor insertion and protein assembly in [NiFe]-hydrogenase biosynthesis. *J. Biol. Chem.* **2017**, *292*, 11670–11681. [[CrossRef](#)] [[PubMed](#)]
49. Senger, M.; Mebs, S.; Duan, J.; Wittkamp, F.; Apfel, U.-P.; Heberle, J.; Haumann, M.; Stripp, S.T. Stepwise isotope editing of [FeFe]-hydrogenases exposes cofactor dynamics. *Proc. Natl. Acad. Sci. USA* **2016**, *113*, 8454–8459. [[CrossRef](#)] [[PubMed](#)]
50. Senger, M.; Mebs, S.; Duan, J.; Shulenina, O.; Laun, K.; Kertess, L.; Wittkamp, F.; Apfel, U.-P.; Happe, T.; Winkler, M.; et al. Protonation/reduction dynamics at the [4Fe–4S] cluster of the hydrogen-forming cofactor in [FeFe]-hydrogenases. *Phys. Chem. Chem. Phys.* **2018**, *20*, 3128–3140. [[CrossRef](#)] [[PubMed](#)]
51. Haumann, M.; Stripp, S.T. The Molecular Proceedings of Biological Hydrogen Turnover. *Acc. Chem. Res.* **2018**, *51*, 1755–1763. [[CrossRef](#)] [[PubMed](#)]
52. Lukey, M.J.; Parkin, A.; Roessler, M.M.; Murphy, B.J.; Harmer, J.; Palmer, T.; Sargent, F.; Armstrong, F.A. How *Escherichia coli* is equipped to oxidize hydrogen under different redox conditions. *J. Biol. Chem.* **2010**, *285*, 3928–3938. [[CrossRef](#)] [[PubMed](#)]
53. Higuchi, Y.; Ogata, H.; Miki, K.; Yasuoka, N.; Yagi, T. Removal of the bridging ligand atom at the Ni-Fe active site of [NiFe] hydrogenase upon reduction with H₂, as revealed by X-ray structure analysis at 1.4 Å resolution. *Structure* **1999**, *7*, 549–556. [[CrossRef](#)]
54. Shafaat, H.S.; Rüdiger, O.; Ogata, H.; Lubitz, W. [NiFe] hydrogenases: A common active site for hydrogen metabolism under diverse conditions. *Biochim. Biophys. Acta* **2013**, *1827*, 986–1002. [[CrossRef](#)] [[PubMed](#)]
55. Soboh, B.; Lindenstrauss, U.; Granich, C.; Javed, M.; Herzberg, M.; Thomas, C.; Stripp, S.T. [NiFe]-hydrogenase maturation in vitro: Analysis of the roles of the HybG and HypD accessory proteins. *Biochem. J.* **2014**, *464*, 169–177. [[CrossRef](#)] [[PubMed](#)]
56. Hartmann, S.; Frielingsdorf, S.; Ciaccafava, A.; Lorent, C.; Fritsch, J.; Siebert, E.; Priebe, J.; Haumann, M.; Zebger, I.; Lenz, O. O₂-tolerant H₂ activation by an isolated large subunit of a [NiFe]-hydrogenase. *Biochemistry* **2018**, *57*, 5339–5349. [[CrossRef](#)] [[PubMed](#)]

